Contact Dynamics Simulation for Space Robotics Applications

Rainer Krenn, Gerd Hirzinger

Abstract—**This paper presents two examples of contact dynamics simulations for space robotics application: Satellite docking in GEO and rover locomotion on planetary surfaces. The contact modeling techniques include a) contact between polygonal surfaces according to the elastic foundation model theory and b) contact between digital elevation grid surfaces and point cloud surfaces with application of Bekker's empirical terramechanics functions. The simulation results, which are taken from the ongoing projects SMART-OLEV (satellite docking simulation) and ExoMars (drawbar pull test simulation), demonstrate that contact dynamics simulations can provide helpful inputs in terms of feasibility confirmation and system design.**

I. INTRODUCTION

D URING the recent years two kinds of spaceflight missions came more and more into the focus of space scientists as well as space engineers:
1) On-orbit servicing missions and
2) Planetary exploration missions.

On-orbit servicing missions offer a variety of service operations at a client spacecraft like station keeping for life time extension purposes, maneuvers for orbit change or well controlled de-orbiting for save removal of old, defective satellites. For performing all these operations the servicing spacecraft has to dock at the client spacecraft and to act as an attached attitude and orbit control unit for a particular time period.

The typical spacecraft system for planetary explorations consists of both, a descend module and a rover that is stowed inside and that will be deployed after landing on the planetary surface. The main task of the rover is transporting scientific payloads to geologically interesting surface locations around the landing site.

Even if the nature of the referred space missions is very different we can state that for both missions the robotics components play crucial roles regarding mission feasibility and success. Robotics gives the systems the required skills for autonomous docking at cooperative and non-cooperative satellite targets as well as the required mobility to deploy and operate scientific instruments at desired locations. And we can further state that the critical phases of both missions are at the times when the robotics systems get in physical contact with their according counterparts, in plain language when the chaser satellite is grasping the target satellite or when the rover wheels are interacting with the soil and rocks of the planetary surface.

A typical way to investigate in those complex physical contact phenomena is extensive experimental testing. However, since the actual operations mentioned above will take place at reduced gravity conditions on planets or at zero-gravity in satellite orbits the required tests can be hardly performed on ground. The main reason is the static load at gravity conditions on earth that many spacecraft structures can mechanically not resist and that change the dynamic behavior of structures and media like sand significantly. In this context numerical simulations of contact mechanics problems offer an elegant solution to avoid those problems rising with gravity on ground. Moreover, the flexibility in terms of test case and parameter variations and last but not least the cost aspect make the software simulations to a very appealing tool for test purposes.

II. ON-ORBIT SERVICING MISSION SMART-OLEV

The on-orbit servicing mission to be mentioned here is the SMART-OLEV mission, where OLEV stands for Orbital Live Extension Vehicle. The mission is based on a tug boat like chaser spacecraft (SMART platform) that is able to dock at a client spacecraft.
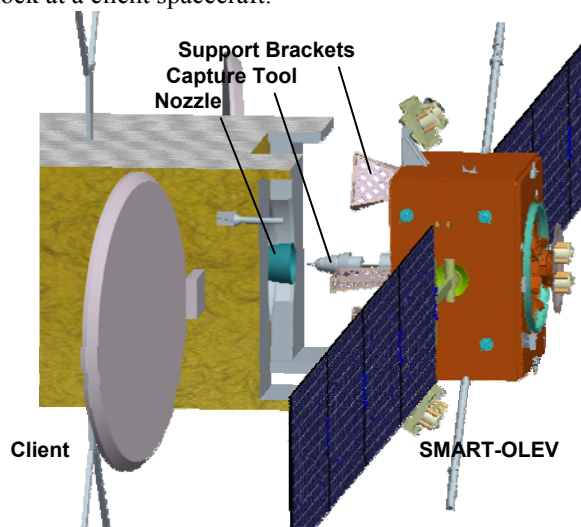

Fig. 1: Satellite Docking Maneuver (Picture: Kayser-Threde)

During the docking maneuver SMART-OLEV deploys a dedicated Capture Tool (CT) on top of an extendable boom (CDM = Capture Tool Deployment Mechanism) into the apogee kick motor nozzle of the client (Fig. 1). Once the CT has reached the nozzle throat the Locking Crown (LC) at the tip of the CT will be spread and creates a rigid mechanical connection with the client. The docking is completed when the boom has been retracted again and client spacecraft is resting with its launch adapter ring on top of three support brackets SB (Fig. 2). After docking SMART-OLEV takes over the AOCS tasks of the mated configuration in order to

extend the operational live time of the client satellite, whose fuel capacity is almost exhausted, by approximately ten years. The project has recently passed the Preliminary Design Review PDR successfully.
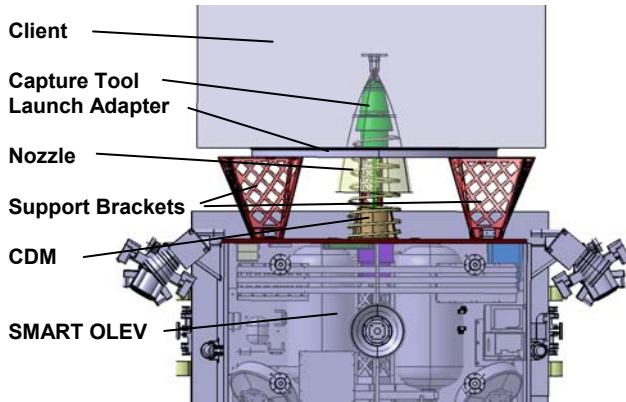

Fig. 2: Mated Configuration of SMART-OLEV and Client (Picture: Kayser-Threde)

A. SMART-OLEV Simulator

For docking simulation purposes a Design Simulator Facility (DSF) has been established in order to support the system and control design as well as the operation and mission analysis. The main components of the simulator that was implemented using Mathlab/Simulink tools are listed below:

- Space environment and satellite dynamics including
  - Flexible, rotating solar panels
  - Reaction wheels and momentum wheels
  - Thrusters
  - AOCS
- Docking payload including
  - Stereo docking camera
  - CDM (modeled as an elastic, extendable boom)
  - CT equipped with distance sensors, contact switches and LC
  - Docking control algorithm

With help of specific docking simulations a number of crucial questions regarding feasibility of docking and mission success had to be answered:

- Is the proposed rendezvous and docking strategy applicable taking into account the proposed docking payload equipment (type of sensors/actuators)?
- Are the specifications of the applied actuators and tools adequate to the requirements of the docking task?
- Are the specifications of the applied sensors sufficient for the requirements of the proposed docking control algorithm?
- Is there any danger for damaging the client satellite or SMART-OLEV when physical contact takes place during docking?
- How does the client satellite dynamically behave when being grasped by the chaser satellite?

In order to be able to answer these kinds of questions the DSF was equipped with a contact dynamics model by DLR that is able to reproduce the characteristics, the amount and the impact direction of the applied contact forces during the physical contact phases of the docking operation.

B. Contact Dynamics Model

The contact dynamics models that were implemented in DSF are derived from the so-called Polygonal Contact Model (PCM, [2]) and adapted to the particular application inside DSF. The general idea of the modeling technique is based on three major steps:

1) Discretization of the contact body surface by polygon meshes and assignment of contact relevant geometric and dynamics parameters individually to each polygon.
2) Detection of polygons, which are in contact with their counter part.
3) Calculation of contact forces/torques based on the relative kinematics states of the contact polygons under respect of the assigned geometric and dynamics parameters.
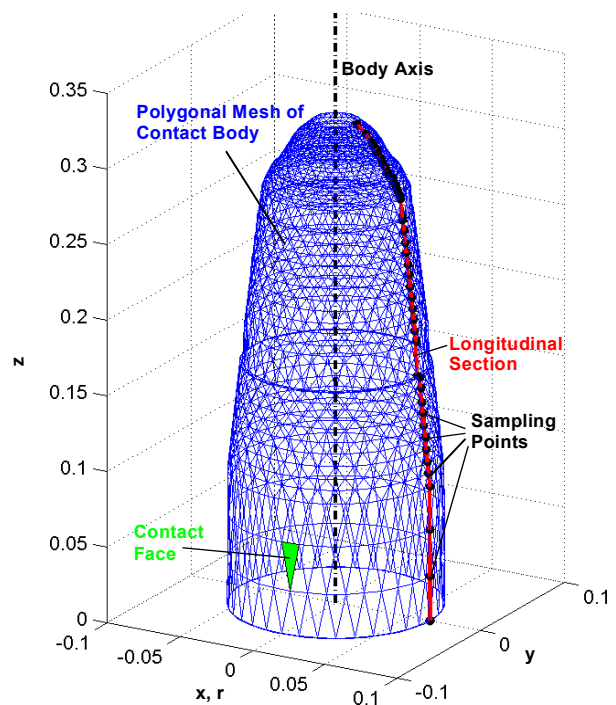
1) Polygonal Contact Surface

Fig. 3: Contact Surface Shape Definition

The method of creating the polygon surface meshes takes advantage of the fact that only rotationally symmetrical surfaces are involved in contact dynamics (Fig. 3). Thus, they can be described by their discrete longitudinal section functions (radius versus axial co-ordinate), which may change its shape if the body is changing its topology during simulation. The distribution of the sampling points depends on the particular curvature of the longitudinal section

function. The higher the curvature, the shorter the distance of the sampling points. These settings guarantee for good sensitivity of the models regarding contact detection at a minimum number of surface polygons. The polygon mesh vertices are created by rotating the longitudinal section around the body axis with discrete angular distances. Within the polygon mesh three adjoining vertices define a so-called face (isosceles triangle).

The next step is the assignment of individual geometric parameters (face area size A, face normal vector $\mathbf{n}$, face center co-ordinates $\mathbf{C}$) and dynamics parameters (normal stiffness c_N, damping d_N, and Coulomb friction for both, stick μ_{stick} and slip μ_{slip}) of the polygonal faces. Regarding the selection of the dynamics parameters we assume elastic surface layers on top of rigid contact bodies such that we can apply the theory of elastic foundation models. The derivation of the dynamics parameters can be found in [2].

2) Contact Detection

In order to detect, if the surface of body B is intersecting the surface of the reference body A (Fig. 4), the according polygon vertex co-ordinates of body B have to be transformed into the body fixed reference frame of body A. In the second step we map the vertices of both bodies into a two-dimensional radial-axial reference frame Fig. 5.

Herein the reference body A appears as its own longitudinal section and the inspected body B as point cloud. And following we can compare the radial vertex co-ordinates of body B with the according values of the longitudinal section function of body A in order to detect contact. From the computation point of view this algorithm is very time-efficient since the number of matrix operation can be reduced drastically compared to contact detection in the three-dimensional space. Moreover, the method can be applied to contact dynamics problems including both, convex and concave bodies and it doesn't cause any limitation in terms of multi-point contact problems.
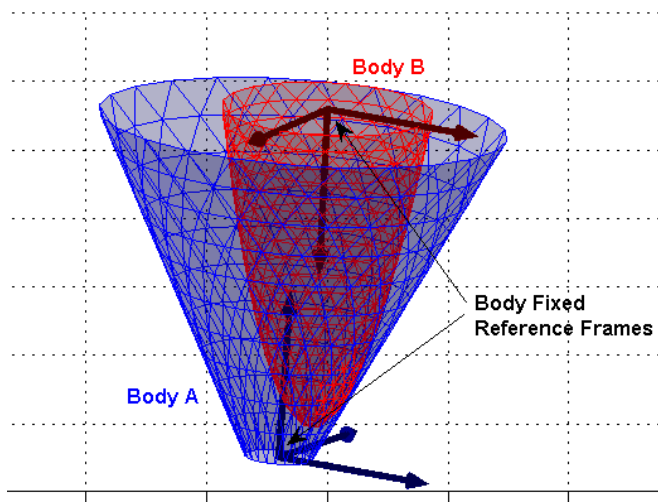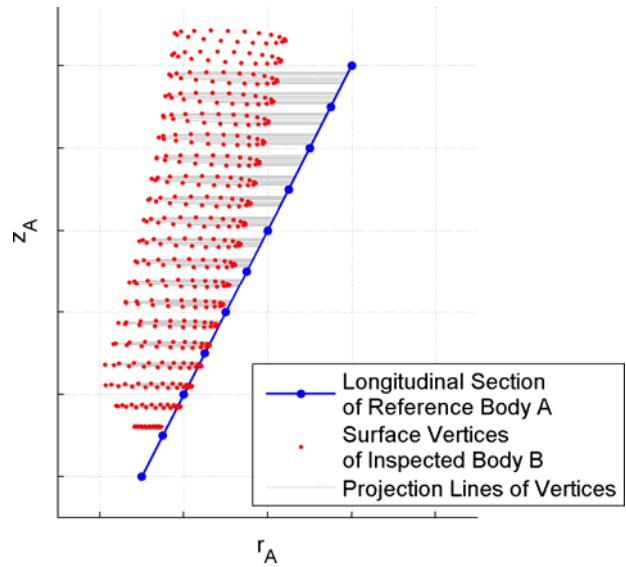

Fig. 4: Contact Shape Definition

Fig. 5: 2D-Projection of Vertices and Contact Detection (Radial)

After re-mapping of the detected contact vertices into the Cartesian space we are able to define the contact shape by the according polygon mesh (Fig. 6). Ambiguous solutions at the border of the contact area (only one or two vertices of a face in contact) will be fixed by refining the affected faces and applying the contact detection to those faces again in an iterative process.
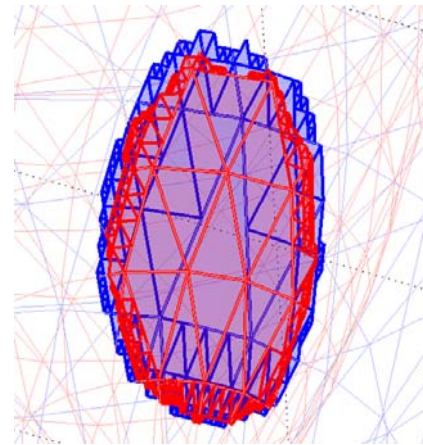

Fig. 6: 3D Contact Shape With Boarder Refinement

3) Contact Forces

For the contact force computation purposes the kinematics states of the contact faces, in particular the normal penetration $\mathbf{s}$, the normal penetration velocity $\mathbf{v}_N$ and the relative tangential velocity $\mathbf{v}_T$, relative to their counterparts have to be calculated. The counterpart faces can be found by projecting the contact shape faces onto the surface of the reference body (Fig. 7).

With the pre-requisites introduced in the previous paragraphs, we are now able to calculate the components of the actual contact forces, individually for each contact face. The normal force is provided by (1). Herein, s_{d0} describes the depth of the transition range wherein the damping forces rise/drop continuously in order to avoid unrealistic adhesive effects as well as step like excitations.
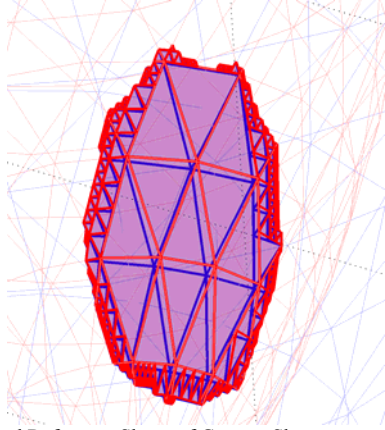
Fig. 7: Mapped Reference Shape of Contact Shape

$$\begin{cases} \mathbf{F}_N = c_N \cdot \mathbf{s} + d_N \cdot \mathbf{v}_N; & |\mathbf{s}| > s_{d0} \\ \mathbf{F}_N = c_N \cdot \mathbf{s} + d_N \cdot \dfrac{|\mathbf{s}|}{s_{d0}} v_N; & 0 > |\mathbf{s}| \le s_{d0} \end{cases} \quad (1)$$

In terms of friction we have to decide about stick or slip and therefore we have to track the current location **r** of the contact face counterpart continuously. The applied force law is described in (2).

$$\begin{aligned} & if \ \ state \ == \ stick \\ & \quad \mathbf{F}_T = c_T \cdot (\mathbf{r} - \mathbf{r}_0) + d_T \cdot \mathbf{v}_T \\ & \quad state = \begin{cases} stick; & \mathbf{F}_T \le \mu_{stick}\mathbf{F}_N \\ slip; & \mathbf{F}_T > \mu_{stick}\mathbf{F}_N \end{cases} \\ & if \ \ state \ == \ slip \\ & \quad \mathbf{F}_T = -\mu_{slip}\mathbf{F}_N \dfrac{\mathbf{v}_T}{|\mathbf{v}_T|} \\ & \quad \mathbf{r}_0 = \mathbf{r} \\ & \quad state = \begin{cases} stick; & |\mathbf{v}_T| < v_{T0} \\ slip; & |\mathbf{v}_T| \ge v_{T0} \end{cases} \end{aligned} \quad (2)$$

It assumes that in stick case the contact face is connected via a tangential spring-damper mechanism (parameters c_T and d_T) with the contact counterpart. Herein $\mathbf{r}_0$ is the tracked location **r** at the time when the friction falls into the stick state and v_{T0} is the according minimum amount of slip velocity. In case of slip friction the model applies the classical Coulomb friction function.

C. Docking Simulation Results

In this paragraph the simulation results of a docking maneuver between SMART-OLEV and a Spacebus 3KB series satellite will be presented. The scope of the results is the contact dynamics between the CT (Fig. 8) including its LC and the nozzle of the client satellite during docking.

The docking maneuver consists of the following steps that can be retraced in the contact force/torque diagrams in Fig. 9.

- 0s - ~40s: In this phase the CDM deploys the CT and inserts it into the client nozzle. At the end the LC passes the nozzle throat. The contact dynamics impact

is negligible in this phase and almost invisible in the diagrams

- ~40s – ~50s: In this phase the LC will be retracted and spread at the same time such the nozzle will be pressed against the shoulder of the CT. The locking force is 100 N. The locking operation is presented in Fig. 10 step by step. In this phase the CT/LC and the nozzle will be aligned with high forces. This operation excites the bending oscillations between the two satellites, which were slightly misaligned at the time of locking.

- 50s - ~220s: The flexible CDM is now connecting the satellites. Its length will be reduced continuously in this phase in order to pull the client towards SMART-OLEV. The oscillations will be slightly damped.

- ~~220s - ~230s: The launch adapter of the client has reached the SB. Since the axes of the adapter and the nozzle are not ideally aligned in terms of orientation the touch down phase is stretched over a couple of seconds. In this phase CDM retraction force starts rising and the CDM obtains an S-like bending, which affects significant lateral forces and torques at the LC.

- ~230s - 300s: The docking is completed when the CDM drive has fully extended a longitudinal safety spring in the CDM that applies additional 200 N at the LC.
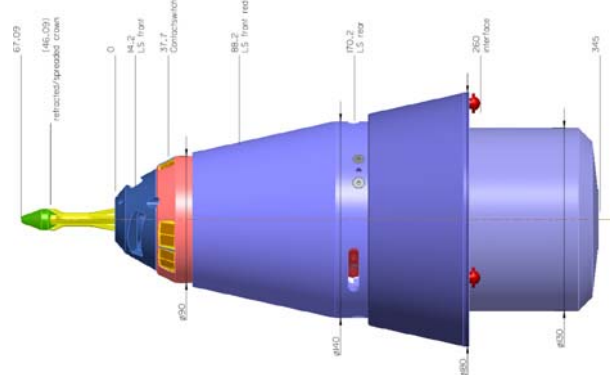

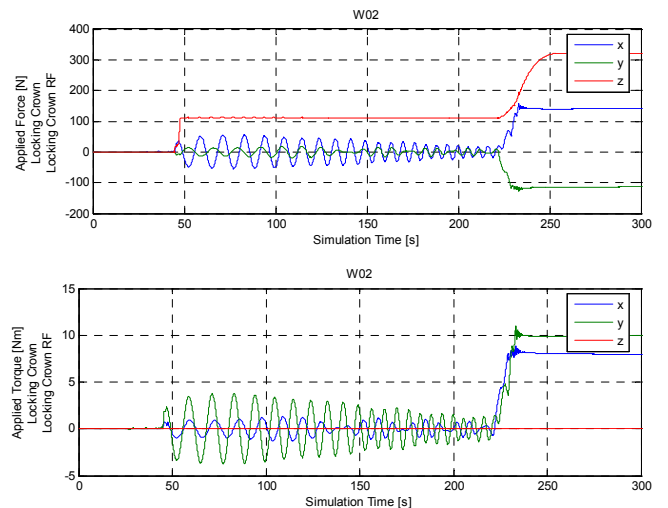Fig. 8: Capture Tool Design

Fig. 9: Contact Forces/Torques at Locking Crown
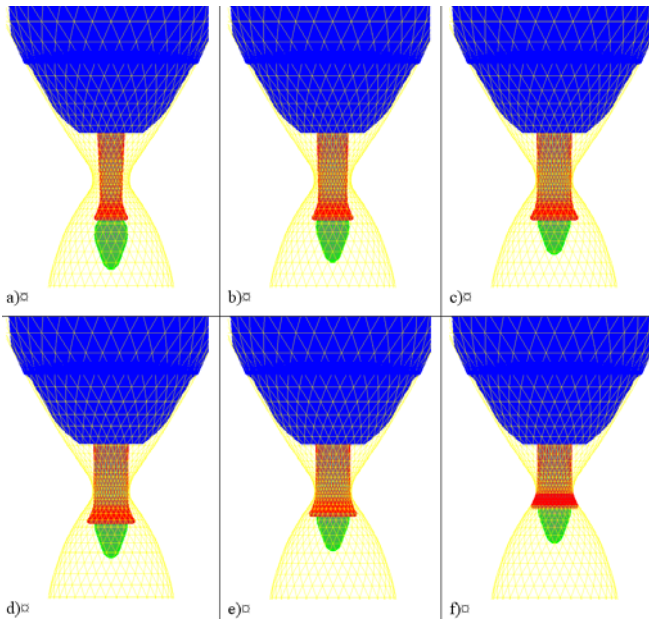(Locking Crown reference frame: x,y = lateral, z = axial)

Fig. 10: Locking Crown Operation

The diagrams in Fig. 11 are documenting details of the contact model during the simulation. Actually, the contact forces presented in Fig. 9 are computed by three contact pairs respectively by three instances of the contact dynamics model:

1) Nozzle – CT body,
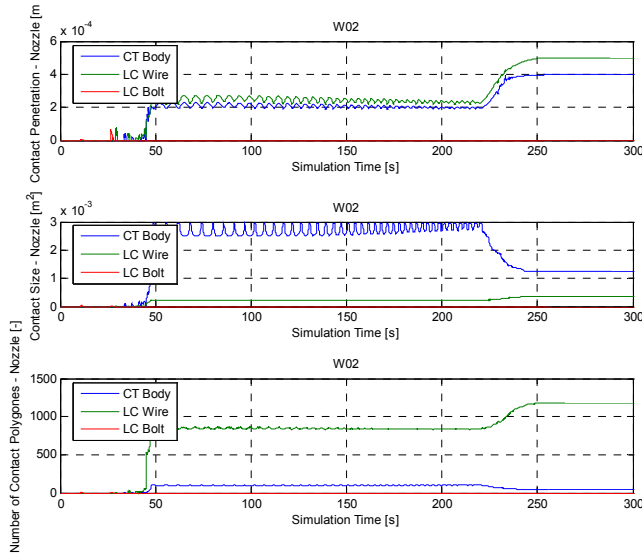2) Nozzle – wire crown of LC,
3) Nozzle – central bolt of LC.

Fig. 11: Contact Model Specific Simulation Results at Locking Crown
(Locking Crown reference frame: x,y = lateral, z = axial)

The diagram on top shows the maximum penetrations of the contact surfaces during the simulation. Since the penetrations are in the same order of magnitude for all contact body pairs and do not exceed 0.5 mm the application of the elastic foundation model theory is assumed to be valid. In the middle diagram the total contact area size is recorded and in bottom one the according numbers of involved contact polygons. Here we see that the polygonal

resolution of the nozzle surface was chosen depending on the contour curvature. In particular around the nozzle throat where the LC wire crown has to adapt to the nozzle shape during contact the resolution is very fine. Therefore, we see a large number of contact polygons at a small total contact area size. Taking all these aspects into account we can expect a quite precise contact force computation.

III. PLANETARY EXPLORATION MISSIONS

In the frame of ESA's ExoMars mission a six-wheel planetary rover is currently under development [3]. For the according chassis test simulations of this rover to be performed at DLR a new modeling technique called Soil Contact Model (SCM) has been developed and implemented in the multi-body simulation (MBS) tool [4].

Fig. 12: Artists Impression of ExoMars Rover (Picture: ESA)

A. Soil Surface Description

The contact problem soil-wheel can be generally described as the contact between a plastically deformable body and a rigid one. This implies that the elastic deformations of the rover wheels are negligible for the dedicated investigations. Therefore we can focus on the soil model description.
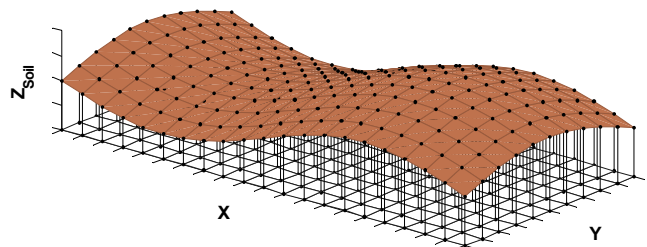

Fig. 13: Soil Elevation Grid

The soil surface inside the SCM algorithm is described as an elevation grid while each grid node can be associated with a number of soil parameters and deformation states.

The most important individual attributes of the grid nodes are collected in Tab. 1.

Tab. 1: Soil Attributes of Grid Node

Parameters	
k_c	cohesive modulus
k_φ	frictional modulus
n	exponent of sinkage
c	cohesion
φ	internal friction
States	
z	plastic vertical soil deformation

B. Contact Detection between Wheel and Soil

For contact detection purposes the wheel is treated as a cloud of surface vertices (Fig. 14, top-left). In the second step we map the horizontal co-ordinates into the grid of the soil such that the vertices will be arranged in columns afterwards (Fig. 14, top-right). Finally, the minimum vertices of each column (Fig. 14, bottom left) will be selected for comparison with the vertical co-ordinates of the according soil grid nodes, respectively to detect contact and to define the footprint (Fig. 14, bottom right). The footprint is the intersection volume of wheel and soil.
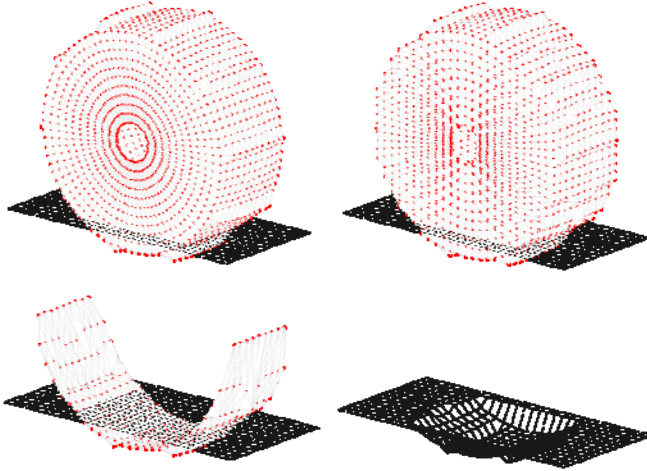

Fig. 14: Contact Detection and Footprint Computation

C. Contact Forces

Once the contact is detected the penetration depth z, the contact area size A, the contact normal vector $\mathbf{n}$ and the relative tangential velocity vector $\mathbf{v}_T$ between wheel and soil have to be calculated for each node of the footprint grid. These are the pre-requisites for the computation of the normal contact forces $\mathbf{F}_N$ (4) and friction forces $\mathbf{F}_T$ (5) according to the empirical formulae of Bekker [5] in (3). Herein, the variable b is representing the width of the wheel.

$$p = \left(\frac{k_c}{b} + k_\varphi\right) z^n \qquad (3)$$

$$\mathbf{F}_N = p \cdot A \cdot \frac{\mathbf{n}}{|\mathbf{n}|} \qquad (4)$$

$$\mathbf{F}_T = -\left(\tan\varphi \cdot |\mathbf{F}_N| + c \cdot A\right) \cdot \frac{\mathbf{v}_T}{|\mathbf{v}_T|} \qquad (5)$$

Implicitly we assume that the maximum transmittable tangential forces are limited by the parameters of the internal soil friction φ and c and not by the coefficient for friction between wheel surface and soil.

D. Plastic Soil Deformation

The implementation of plastically deformable soils, respectively the footprint and landfill computation in the contact model was motivated by the rover simulation task. While cruising we have leading rover wheels, driving through untouched soil with a significant bulldozing effect while the wheels following inline can drive on top of the pre-compressed soil at lower rolling resistance (multi-pass). Moreover, it should be possible to simulate self-carving of the wheels into the soil under adverse conditions.

A further motivation is caused by the nature of the elevation grid based soil model. Herein a classical shear stress–strain relation according to Janosi and Hanamoto [6] is hardly implementable since only vertical degrees of freedom for the soil deformation are provided by SCM. On the other hand, shear deformations of the soil inside the model are only possible in connection with vertical penetrations of contact objects. Therefore, an appropriate soil deformation algorithm can provide equivalent stress–strain relations as described in the empirical functions.

The algorithm for the plastic soil deformation, which is currently a first approach, is inspired by computer graphics solutions algorithms for terrain generation (e.g. Olsen [7]) and animating footprints in soil (e.g. Sumner et al. [8]). and consists of three steps:

1) Soil Displacement

The total volume of the soil displacement is equal to the volume of the footprint that has been created by the contact body (Fig. 14, bottom right). This implies that the soil height reduction is equal to the wheel sinkage z at the according grid node. The displaced volume is divided into three parts depending on the relative kinematics (relative velocity $\mathbf{v}$ with its normal and tangential components $\mathbf{v}_N$ and $\mathbf{v}_T$) between soil and contact body. The parts are caused by sinkage (6), bulldozing (7) and shearing (8).

$$V_{Sinkage} = zA \cdot \frac{\mathbf{v}_N^T \begin{pmatrix} 0 & 0 & 0 \\ 0 & 0 & 0 \\ 0 & 0 & 1 \end{pmatrix} \mathbf{v}_N}{\mathbf{v}^T \mathbf{v}} \qquad (6)$$

$$V_{Bulldozing} = zA \cdot \frac{\mathbf{v}_N^T \begin{pmatrix} 1 & 0 & 0 \\ 0 & 1 & 0 \\ 0 & 0 & 0 \end{pmatrix} \mathbf{v}_N}{\mathbf{v}^T \mathbf{v}} \qquad (7)$$

$$V_{Shear} = zA \cdot \frac{\mathbf{v}_T^T \mathbf{v}_T}{\mathbf{v}^T \mathbf{v}} \qquad (8)$$

2) Temporary Soil Deposition

In this step the displaced soil volume will be temporary distributed over the border grid nodes of the footprint. So each border node gets a certain portion of each footprint node. The individual weighting factor w indicating how big the portion will actually be depends on the distance vector $\mathbf{d}$ from the footprint node to border node for sinkage (9) and the angle α between $\mathbf{d}$ and $\mathbf{v}$ for bulldozing and shearing (10).

$$w_{Sinkage} = \frac{1}{\mathbf{d}^T \mathbf{d}} \qquad (9)$$

$$w_{Bulldizing} = w_{Shear} = \begin{cases} 0; & \cos\alpha \le 0 \\ \cos\alpha^m; & \cos\alpha > 0 \end{cases}$$

$$\text{with} \quad \cos\alpha = \frac{\mathbf{d}^T \mathbf{v}^T}{|\mathbf{d}| \, |\mathbf{v}|}; \quad m > 1$$

$$(10)$$

An impression for soil displacement and temporary deposition is given in Fig. 15. Here a wheel was rolling over the soil with a constant sinkage rate.
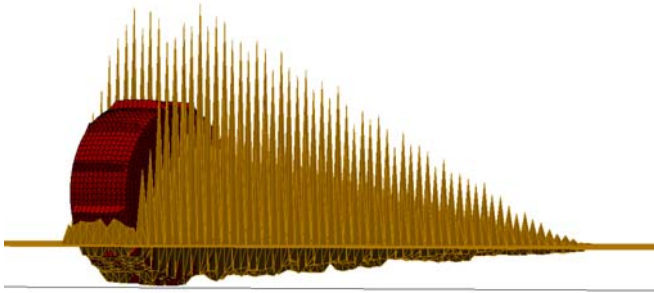

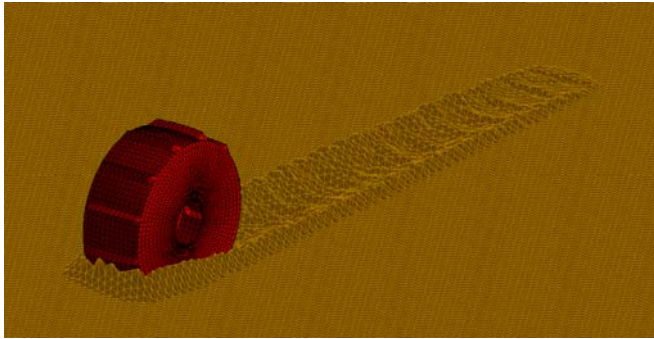Fig. 15: Soil Displacement and Temporary Deposition without Erosion

Fig. 16: Soil Displacement, Deposition and Erosion

3) Erosion of Soil

When sand is piled a maximum sand hill slope angle can be achieved, which is equal to the internal friction angle φ of the sand. Therefore, after temporary deposition of the displaced soil volume an erosion algorithm will be applied to the soil grid nodes in the vicinity of the contact area in order to meet this physical limitation. At soil grid resolution ds the maximum soil height difference to the n adjacent nodes is limited as given in (11).

$$dz_{Limit} = ds \cdot \tan\varphi \qquad (11)$$

In the erosion algorithm (12) half of the height that exceeds dz_{Limit} will be removed and added to the adjacent nodes according to their individual fraction of the total erosion potential.

$$dz_{erosion,i} = -\frac{\max(dz_i) - dz_{Limit}}{2} \cdot \frac{dz_i}{\sum\limits_{i=1}^{n} dz_i}; \quad i = 1, 2, \cdots, n \qquad (12)$$

In Fig. 16 the result of the complete plastic soil deformation process is present.

E. Simulation Results

In the following paragraph simulation results of a drawbar pull test will be presented exemplarily. Fig. 17 shows the scenario of the test: The ExoMars rover equipped with six actuated wheels has to move in a straight line on top of a flat terrain. Hereby, the rover chassis is connected with a linear spring acting as a drawbar pull force sensor. The total test takes three minutes. The simulated gravity is equal to the gravity on Mars.
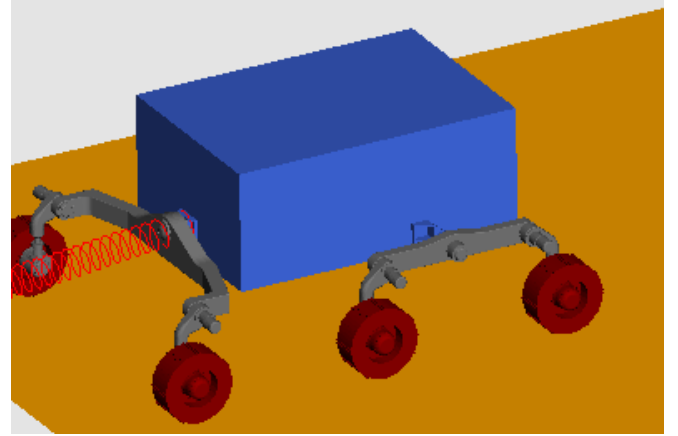

Fig. 17: Drawbar Pull Simulation Scenario (Initial Conditions);
Soil Properties: kc = 2370; kφ = 60300; n = 0.63; b = 0.1

In Fig. 18 the sinkage of the wheels during the test is presented. The rover drops into the sand at time $t = 0$ and in the first 10 seconds the rover passes over the sand hills around its wheels caused the initial sinkage. In the following time the rover moves forward and stretches continuously the attached spring.
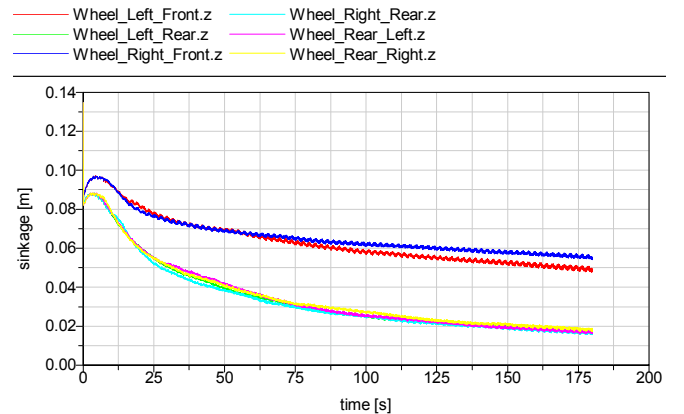

Fig. 18: Wheel Sinkage

The spring force (drawbar pull) causes slippage of the wheels and therefore the wheels are digging themselves

more and more into the soil. In Fig. 18 the according sinkage functions are presented. We can easily identify that the sinkage of the front wheels (left bogie front, right bogie front) is significantly less than of those of the middle and rear wheels. The reasons for this behavior are the location of the rover's center of mass as well as the kinematics of the bogies.
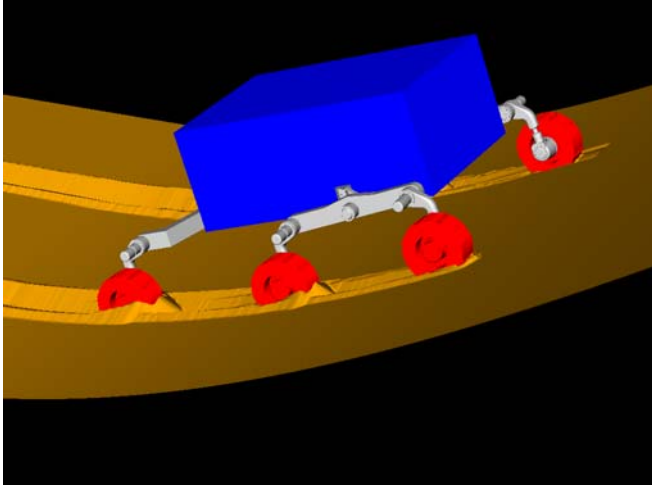

Fig. 19: Uphill Gradability Test

The simulations of the rover uphill gradability generate similar results (Fig. 19 with 3D-animation of wheel sinkage and soil deformation).
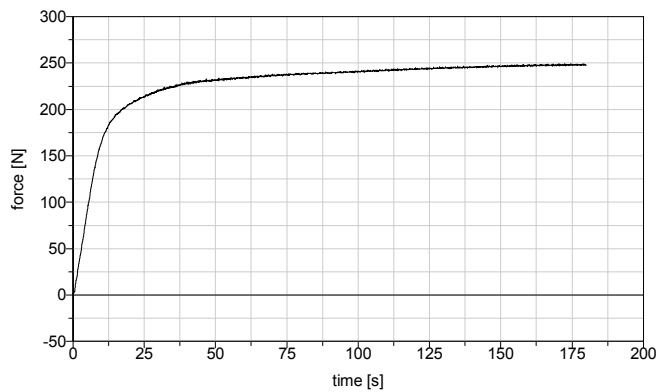

Fig. 20: Drawbar Pull

The simulated drawbar pull function (Fig. 20) has the typical shape known from experimental testing. Two effects can be clearly demonstrated: The rising drawbar pull force at rising slippage of the wheels and the asymptotic approach of the drawbar pull force towards a maximum value.

IV. CONCLUSION

In the paper two contact dynamics modeling techniques applied for space robotics applications were presented: One for hard physical contact cases and one for contact with plastically deformable media. Both methods have been implemented in multi-body dynamics simulation tools. In the paper each method was presented in the frame of a specific simulation task. However, since the implementation

technique is very similar, both types of models can run in parallel as well. Following this option we started recently to develop a simulation environment for rover locomotion in rocky and sandy terrain. A first simulation result using the Polygonal Contact Model (PCM) for the contact dynamics between wheels and rocks and the Soil Contact Model for the interaction between wheels and sand is presented in Fig. 21.
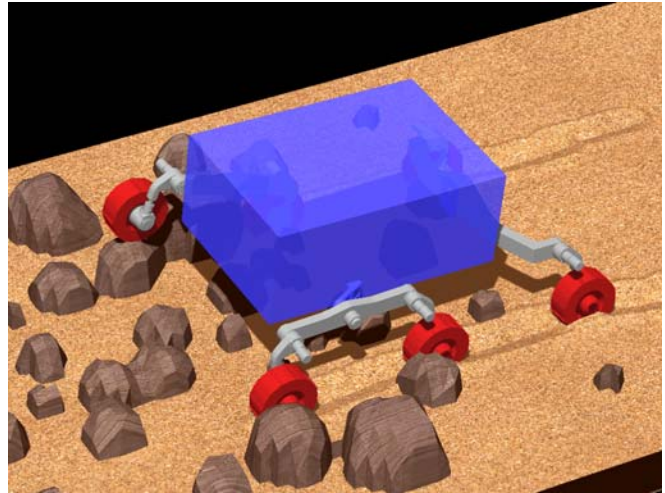

Fig. 21: Simulation Result Using PCM and SCM

REFERENCES

[1] C. Kaiser, F. Sjöberg, J,-M. del Cura, B. Eilertsen: "SMART-OLEV – An Orbital Life Extension Vehicle for Servicing Commercial Spacecrafts in GEO", 58th IAF Congress, 24.-28. September 2007, Hyderabad, India, IAF-Paper IAC-07-D1.1.06

[2] G. Hippmann, "Modellierung von Kontakten komplex geformter Körper in der Mehrkörpersimulation", Dissertation, TU Wien, 2004.

[3] M. Van Winnendal, P.Baglioni, A. Elfing, F. Ravera, J.Clemmet and E. Re, "The ExoMars Rover – Overview of Phase B1 Results", 9th Int. Symposium on Artificial Intelligence Robotics and Automation in Space iSAIRAS 2008, February 25-29, 2008, Los Angeles, USA

[4] www.simpack.de

[5] M.G. Bekker, "Introduction to Terrain-Vehicle Systems", The University of Michigan Press, Ann Arbor, USA, 1969.

[6] Z. Janosi and B. Hanamoto, "Analytical Determination of Drawbar Pull as a Function of Slip for Tracked Vehicles in Deformable Soils", 1st Int. Conference on Terrain-Vehicle Systems, Turin, Italy, 1961

[7] J. Olsen, "Realtime Procedural Terrain Generation", IMADA, University of Southern Denmark, 31 October, 2004

[8] R.W. Sumner, J.F. O´Brien and J.K. Hodgins, "Animation Sand, Mud and Snow", Computer Graphics Forum, Volume 18, No 1, 1999